

# Inverse Faraday effect in $3d$ , $4d$ and $5d$ transition metals

Shashi B. Mishra\*

*Mechanical Engineering, University of California, Riverside, California 92521, USA.*<sup>†</sup>

(Dated: November 21, 2024)

Using first-principles calculations, we systematically investigate the spin contributions to the inverse Faraday effect (IFE) in transition metals. The IFE is primarily driven by spin-orbit coupling (SOC)-induced asymmetry between excited electron and hole spin moments. Our results reveal that even elements with smaller electron magnetic moments, like Os, can exhibit higher IFE due to greater electron-hole asymmetry. Pt shows the highest IFE in the 1–2 eV frequency range, while Os dominates in the 2–4 eV range. In addition, we demonstrate that the IFE of neighboring elements with similar crystal structures (e.g., Ir, Pt, and Au) can be tuned by adjusting their Fermi levels, indicating the importance of  $d$  electron filling on IFE. Finally, we find that the trend in electron (or hole) contributions to the IFE closely follows that of the spin Hall conductivity (SHC), however, the total IFE involves more complex interactions.

## I. INTRODUCTION

The inverse Faraday effect (IFE) is a nonlinear optical phenomenon where circularly polarized light (CPL) induces magnetic moments in a material without requiring an external magnetic field [1, 2]. This ability enables all-optical helicity-dependent switching (AO-HDS) [3–5]. Experimentally, IFE has been shown to reverse the magnetization of ferrimagnets with a strong laser pulse [6, 7] and allows laser light to exert torques on magnetic metals [8]. Given these capabilities, IFE holds significant potential for applications in ultrafast magnetism [9] and magneto-optics [10, 11].

The IFE was first described phenomenologically in the 1960s [12, 13]. Later, it was revisited, and a model for IFE in an isotropic, collisionless electron plasma was derived [14]. To better understand the behavior in real materials, several quantum mechanical theories of IFE have been proposed, particularly for magnetic metals [15–18]. For non-magnetic metals with inversion symmetry, special attention is needed due to the doubly degenerate nature of their electronic bands. In our previous work [19], we developed a gauge-invariant IFE theory that accounts for the induced spin contributions in such materials.

In this study, we examine the spin contributions to the IFE in  $3d$ ,  $4d$ , and  $5d$  transition metals to understand how various material properties influence the IFE and identify the key parameters governing it. Since most elements in these series are non-magnetic, except for Fe, Co, and Ni, we consider non-magnetic structures for all elements to analyze trends in the IFE as a function of valence electrons. The IFE in magnetic systems, which involves contributions from intraband excited electron-hole moments, will be explored in future work.

Recently, there has been growing interest in studying trends in the spin Hall effect (SHE) and orbital Hall effect (OHE) among transition metals [20–24]. As we move

across the periodic table, the number of valence electrons increases. However, as we move down the table from  $3d$  to  $4d$  and  $5d$  elements, both the spin-orbit interaction and  $d$ -band width increase, even though the number of valence electrons remains constant. Previous studies have shown that the SHE increases with the number of valence electrons and becomes more pronounced in metals with stronger SOC, whereas the OHE exhibits more complex behavior. To our knowledge, no prior studies have systematically explored how the IFE varies with the number of valence electrons.

We analyzed the IFE for 30 transition metals using the expression outlined in Eq. (1), which accounts for contributions from both excited electron and hole moments. Interestingly, we found that the trend in electron moments closely aligns with that of the SHC, where a transverse electric field generates a spin current [20, 25]. However, the total IFE is governed by more intricate factors, particularly the subtle asymmetries between the magnetic moments of excited electrons and holes. These asymmetries are influenced by spin-orbit interaction and the electronic structure of the materials. This mechanism is conceptually similar to the anomalous Hall effect (AHE) in ferromagnets, where an imbalance in the magnetic moments of conduction electrons, driven by SOC, produces a transverse voltage in response to an electric field [20, 26]. In the case of IFE, the SOC-driven asymmetry between excited electron and hole moments determines both the magnitude and sign of the effect.

Among the metals studied, Pt exhibits the highest spin IFE in the 1–2 eV frequency range, while Os shows the largest IFE in the 2–4 eV range but with an opposite sign to that of Pt. We also demonstrated that the IFE values of Ir and Au can be made analogous with that of Pt by adjusting their Fermi levels. Such tuning of the Fermi level can be achieved through practical methods such as metal doping or alloying, offering a promising way to manipulate the IFE in these materials.

\* [mshashi125@gmail.com](mailto:mshashi125@gmail.com)

<sup>†</sup> Current address: Department of Physics, and Astronomy, Binghamton University-SUNY, Binghamton, New York 13902, USA

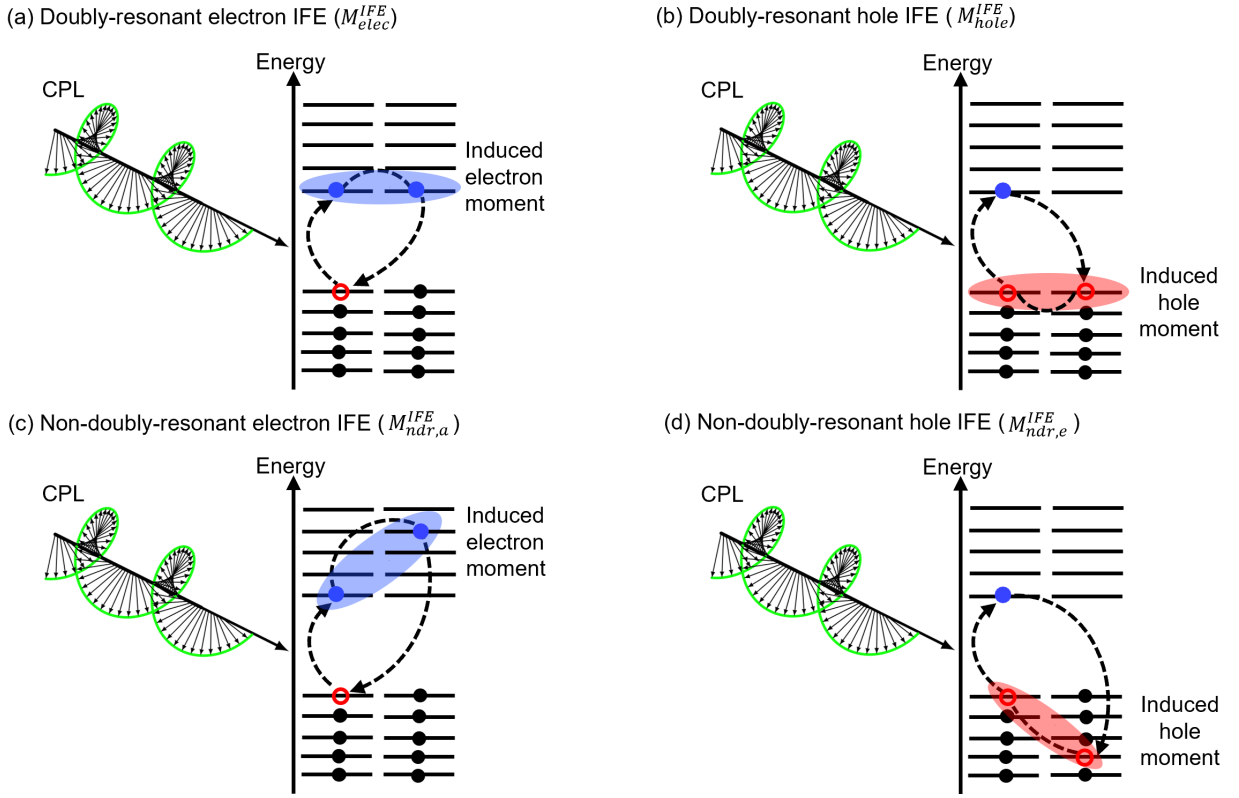


FIG. 1. Schematic illustration of the dominant contributions to the IFE in metals with doubly degenerate band structures. Band doublets are represented by two solid lines at each energy level. Panels (a) and (b) depict the doubly-resonant contributions to the IFE from excited electron ( $M_{elec}^{IFE}$ ) and hole ( $M_{hole}^{IFE}$ ) moments, respectively. Panels (c) and (d) illustrate the dominant non-doubly-resonant contributions from electrons ( $M_{ndr,a}^{IFE}$ ) and holes ( $M_{ndr,e}^{IFE}$ ), respectively.

## II. THEORY

The IFE is a second-order response of a material to an external electromagnetic field. Its theory has been derived using either the density matrix approach [27] or a perturbative formalism [19, 28]. Both methodologies calculate the IFE by summing over occupied (valence) and empty (conduction) states, a technique known as the sum-over-states method. A key consideration is how this sum is affected by band degeneracy. For instance, in nonmagnetic metals with inversion symmetry, the bands are doubly degenerate [29], corresponding to spin-up and spin-down states in the absence of SOC. With SOC, these states are still degenerate but cannot be distinctly labeled. The use of sum-over-states poses challenges in such doubly degenerate bands [30], particularly in the second-order perturbation calculations of the IFE [19].

To address this, we define each state by the index  $n$  and a sub-index  $N$  to distinguish the doublets. For each  $n$ , the states  $N = 1$  and  $N = 2$  represent the two parts of the doublet, corresponding to the same eigenenergy  $E_{n\mathbf{k}} = E_{nN\mathbf{k}}$ , with  $\mathbf{k}$  as the crystal momentum  $\mathbf{k}$ . The doublets are depicted schematically by solid lines in Fig. 1. The Bloch states for these doublets are denoted as  $|\phi_{nN\mathbf{k}}\rangle$ .

The IFE for such a system can be decomposed into three distinct terms as shown below [19]:

$$M^{IFE} = M_{elec}^{IFE} - M_{hole}^{IFE} + M_{ndr}^{IFE}. \quad (1)$$

Here,  $M_{elec}^{IFE}$  and  $M_{hole}^{IFE}$  represent doubly resonant excited electron and hole spin moments. These terms are expressed through the integrals within the first Brillouin zone (BZ) as follows.

$$M_{elec}^{IFE} = \int_{\text{BZ}} \frac{d^3k}{(2\pi)^3} \sum_n^{\text{occ}} \sum_{N=1}^2 \sum_m^{\text{emp}} \sum_{M=1}^2 \sum_{M'=1}^2 \frac{\langle \phi_{nN\mathbf{k}} | V | \phi_{mM\mathbf{k}} \rangle \langle \phi_{mM\mathbf{k}} | M^{\text{spin}} | \phi_{mM'\mathbf{k}} \rangle \langle \phi_{mM'\mathbf{k}} | V^\dagger | \phi_{nN\mathbf{k}} \rangle}{(E_{m\mathbf{k}} - E_{n\mathbf{k}} - \hbar\omega)^2 + \eta^2}, \quad (2)$$

$$M_{hole}^{IFE} = \int_{\text{BZ}} \frac{d^3k}{(2\pi)^3} \sum_n^{\text{occ}} \sum_{N=1}^2 \sum_{N'=1}^2 \sum_m^{\text{emp}} \sum_{M=1}^2 \frac{\langle \phi_{nN\mathbf{k}} | V | \phi_{mM\mathbf{k}} \rangle \langle \phi_{mM\mathbf{k}} | V^\dagger | \phi_{nN'\mathbf{k}} \rangle \langle \phi_{nN'\mathbf{k}} | M^{\text{spin}} | \phi_{nN\mathbf{k}} \rangle}{(E_{m\mathbf{k}} - E_{n\mathbf{k}} - \hbar\omega)^2 + \eta^2}. \quad (3)$$

The electric field of the incident light is assumed to be in the  $x$ - $y$  plane, inducing the magnetic moment along the  $z$ -direction. The spin matrix elements are given by,  $\langle \phi_{mM\mathbf{k}} | M^{\text{spin}} | \phi_{mM'\mathbf{k}} \rangle = 2 \frac{e}{2m_e} \langle \phi_{mM\mathbf{k}} | S_z | \phi_{mM'\mathbf{k}} \rangle$ . The interband transition matrix ( $n \neq m$ ) elements are:  $\langle \phi_{nN\mathbf{k}} | V | \phi_{mM\mathbf{k}} \rangle = \frac{e}{2} \sqrt{\frac{I}{\epsilon_0 c}} \frac{E_{n\mathbf{k}} - E_{m\mathbf{k}}}{\hbar \omega} (A_{nNmM\mathbf{k}}^x + iA_{nNmM\mathbf{k}}^y)$ , where  $A_{nNmM\mathbf{k}}^\alpha$  is the Berry connection matrix,  $e$  is the charge of the electron,  $I$  is the intensity of the incoming light,  $c$  is the speed of light,  $\epsilon_0$  is the permittivity of the free space, and  $\eta$  is the lifetime of the excited electron. For a detailed derivation, please see Ref. [19].

In Eq. (2), sums over  $N$ ,  $M$ , and  $M'$  are performed within the doublet subspace. When  $E_{n\mathbf{k}} - E_{m\mathbf{k}} = \hbar\omega$ , a resonance peak appears. Since IFE is a non-linear response, if the second transition occurs between states that are very close in energy, i.e., among the band-doublets, we observe double-resonances, represented as  $M_{\text{elec}}^{\text{IFE}}$  and  $M_{\text{hole}}^{\text{IFE}}$  corresponding to electron and hole spin moments. These terms are schematically shown in Figs. 1(a) and 1(b), respectively.

Conversely, if the second transition involves states that are not close in energy, it is represented as non-doubly-resonant term  $M_{\text{ndr}}^{\text{IFE}}$ . In our previous work [19], we showed that  $M_{\text{ndr}}^{\text{IFE}}$  contains eight terms. Among these, two most dominant terms are  $M_{\text{ndr,a}}^{\text{IFE}}$  and  $M_{\text{ndr,e}}^{\text{IFE}}$ , illustrated in Figs. 1(c) and 1(d), respectively.

### III. COMPUTATIONAL METHODS

We performed density functional theory calculations using Quantum ESPRESSO [31] within the generalized gradient approximation [32]. We used fully relativistic ONCV pseudopotentials [33] from the pseudo-dojo library [34]. The kinetic energy cutoff for the plane wave basis expansion was set to 120 Ry. We used experimental lattice parameters for all metals. We considered body-centered cubic (bcc) structures for V, Cr, Mn, Fe, Nb, Mo, Ta, and W, and face-centered cubic (fcc) structures for Ni, Cu, Rh, Pd, Ag, Ir, Pt, and Au. The bcc and fcc structures contain one atom in the primitive lattice. We considered hexagonal-close-packed (hcp) structures for Sc, Ti, Co, Y, Zr, Tc, Ru, Lu, Hf, Re, Os, Zn, and Cd, which have two atoms in the primitive cell. For Hg, we used the solid rhombohedral structure, which had two atoms in the primitive cell.

We performed self-consistent calculations using  $\mathbf{k}$ -meshes of  $24 \times 24 \times 24$  for fcc and bcc structures, and  $16 \times 16 \times 16$  for hcp metals. Non-self-consistent calculations were performed using  $8 \times 8 \times 8$   $\mathbf{k}$ -grid. We constructed 18 atom-centered Wannier orbitals  $sp^3d^2$ ,  $d_{xy}$ ,  $d_{yz}$ , and  $d_{zx}$  for fcc and bcc metals, and 36 Wannier functions for hcp metals, using Wannier90 [35, 36]. We used the Wannier Berri [37] package for Wannier interpolation [38]. We found that a  $\mathbf{k}$ -point interpolation grid of  $100 \times 100 \times 100$  is sufficient to obtain the convergence

for fcc and bcc metals, while for hcp structures, we used  $\mathbf{k}$ -meshes of  $70 \times 70 \times 70$ . To avoid singular points in the Brillouin zone with high symmetry, we shifted the uniform interpolation grid by a small random displacement along all three cartesian directions. We used a constant inverse lifetime ( $\eta$ ) of 0.1 eV in our calculations. We calculated the spin hall conductivity (SHC) for these metals with electric fields in the  $x - y$  plane so that the spin polarizations are along the  $z$  direction. We performed SHC calculations at  $\omega = 0$  with  $\eta = 0.1$  eV using Wannier Berri [37, 39].

## IV. RESULTS

### A. Frequency dependence of IFE in 3d, 4d, and 5d metals

We investigate the spin contributions to the IFE in 3d, 4d, and 5d transition metals. The frequency dependence of the IFE,  $M^{\text{IFE}}$ , and its decomposition into doubly-resonant terms,  $M_{\text{elec}}^{\text{IFE}} - M_{\text{hole}}^{\text{IFE}}$ , and non-doubly-resonant terms,  $M_{\text{ndr}}^{\text{IFE}}$ , as expressed in Eq. (1) are plotted in Figs. 11–13 of Appendix A. For most elements, especially 5d metals where SOC is stronger compared to 3d and 4d metals, the contributions from the doubly-resonant terms are larger than those from the non-doubly-resonant terms. When the valence electrons are fully filled, as in Zn, Cd, and Hg, the doubly-resonant and non-doubly-resonant terms are similar in magnitude but opposite in sign, resulting in a negligible total spin IFE. This occurs because when the outer  $d$  and  $s$  states are fully occupied, there is less asymmetry between the electron and hole spin moments, reducing the magnitude of the doubly-resonant term. Similar observations have been reported in the literature for spin-Hall conductivity (SHC) calculations [23, 24].

### B. Average IFE as a function of valence electrons

To quantitatively analyze the trend of IFE with valence electrons, we divide the frequency range into three regimes: 1–2, 2–3, and 3–4 eV. In each regime, we calculate the average IFE, with the results shown in Fig. 2. The general trend in IFE with valence electrons is similar across 3d, 4d, and 5d metals. However, as SOC increases with the atomic number [40, 41], the IFE values of 5d metals are higher than those of 3d and 4d metals. For instance, in the 1–2 eV regime, the IFE ratio between Pt and Pd is proportional to the fourth power of their atomic numbers ratio. We further observe that IFE values are higher for the late transition metals with 8, 9, and 10 valence electrons, indicating the importance of filling  $d$  states near the Fermi energy. However, predicting the precise dependence of IFE on atomic numbers across all 30 elements is challenging due to the complex nature of IFE expression (see Eq. 1). As we move from

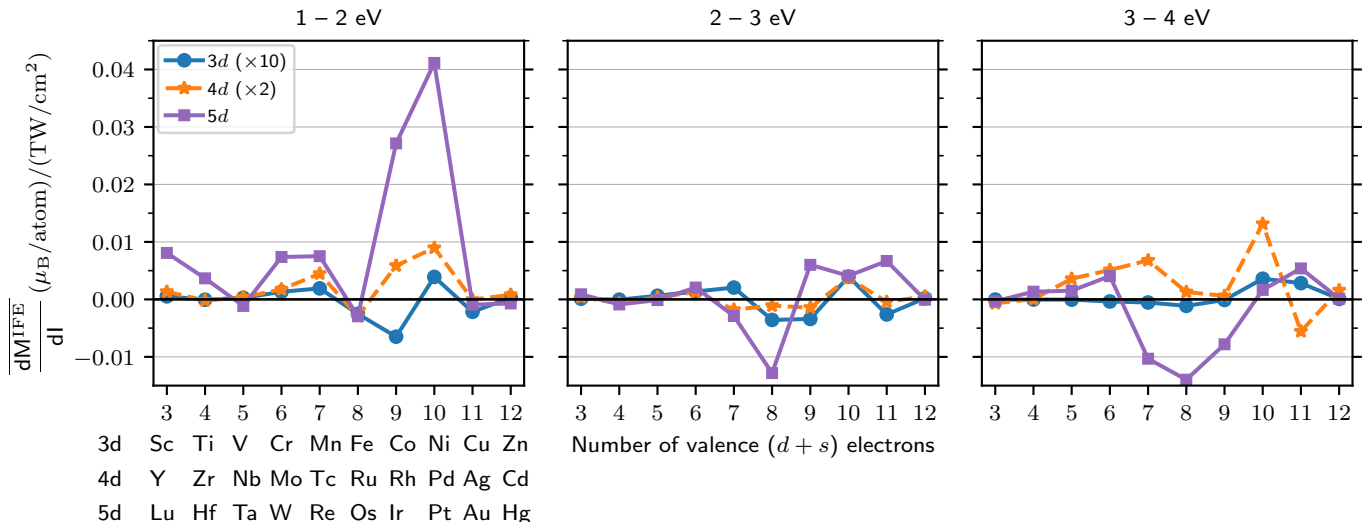


FIG. 2. Average spin IFE for 3d, 4d, and 5d metals as a function of valence ( $d+s$ ) electrons. The frequency dependence of IFE is given in Figs. 11–13 of the Appendix A. The IFE is averaged over three frequency ranges: 1–2 eV (left), 2–3 eV (middle), and 3–4 eV (right). For visibility, we scaled the IFEs for 3d and 4d metals by ten and two factors, respectively.

1–2 eV to 2–4 eV frequency range, the IFE competes with the prefactor  $1/\omega^2$  (see Eq. 17 of Ref. 19) and interband resonance peaks, which depend on the element’s band structure. For example, Os and Au exhibit  $d \rightarrow s$  interband resonance peaks above 2 eV (see Fig. 13 in Appendix A), resulting in a larger IFE in the 2–4 eV range compared to the 1–2 eV range.

Based on the IFE trends, we classify these 30 elements into four groups. The first group includes early transition metals (groups 3, 4, and 5) with outer  $d$  orbitals containing one, two, and three electrons, respectively. IFE decreases as we move from group 3 to groups 4 and 5 in the 1–2 eV range. The second group comprises groups 6 and 7, with nearly half-filled  $d$  orbitals. The IFEs of these elements are larger than those of the preceding groups. Notably, elements in group 6 exhibit larger magnitude of  $M_{\text{elec}}^{\text{IFE}}$  and  $M_{\text{hole}}^{\text{IFE}}$  compared to groups 5 and 7 (Fig. 4).

In the third group, which includes elements from groups 8, 9, and 10, the outer  $d$  orbitals contain six, seven, and eight electrons, respectively. Elements in group 8 generally show negative IFE values, with Os exhibiting the highest IFE among all metals in the 2–4 eV regime. Group 10 elements, such as Ni, Pd, and Pt, exhibit higher positive IFE in the 1–2 eV range, with Pt showing the highest spin IFE among all metals in this range due to its nearly filled  $d$  states and strong SOC. The fourth group includes elements from groups 11 and 12, characterized by electrons in the  $s$  bands and filled  $d$  bands. For group 11 elements, IFE increases near the  $d \rightarrow s$  transition region; for example, Au shows a significant increase above 2 eV, and Ag has a peak around 3 eV, driven by interband optical resonances [42–45] (see Appendix A). Group 12 elements with filled  $d$  and  $s$  states exhibit lower IFEs due to the near cancellation of doubly

resonant and non-doubly resonant terms.

To gain insights into the IFE trend with electrons, we examine various parameters such as the number of optical transitions, the doubly-resonant electron and hole terms, and the spin-orbit-driven asymmetry of excited electron-hole spin moments discussed in the following sections.

### C. Analysis of average IFE with JDOS/ $\omega^2$

The IFE describes the induced magnetic moments generated by the interaction of excited electrons or holes with CP light. We expect that the IFE would increase with greater optical transitions from occupied to empty states, represented by the joint density of states (JDOS) (see Fig. 1). In our previous study [19], we found that, for a simple metal like fcc Au, the frequency dependence of the doubly-resonant electron IFE ( $M_{\text{elec}}^{\text{IFE}}$ ) or the hole term IFE ( $M_{\text{hole}}^{\text{IFE}}$ ) resembles JDOS/ $\omega^2$  behavior. To further explore the relationship between IFE and JDOS, we plot the mean absolute value of the IFE against the mean JDOS/ $\omega^2$  within each frequency regime in Fig. 3. It shows that, across each regime, variations in IFE among different elements do not correlate with JDOS variations. For instance, in the 1–2 eV regime, we highlight three representative 5d metals, such as Ta, Ir, and Pt. They have similar JDOS values, however the IFE of Ir and Pt is an order of magnitude larger than that of Ta. This trend is also seen among other 3d, 4d, and 5d elements, suggesting that a higher JDOS does not necessarily result in a higher IFE.

To further understand the trends in IFE, we analyze the doubly-resonant terms  $M_{\text{elec}}^{\text{IFE}}$ ,  $M_{\text{hole}}^{\text{IFE}}$ , and their asymmetric spin moment ( $M_{\text{elec}}^{\text{IFE}} - M_{\text{hole}}^{\text{IFE}}$ ) in the following sec-

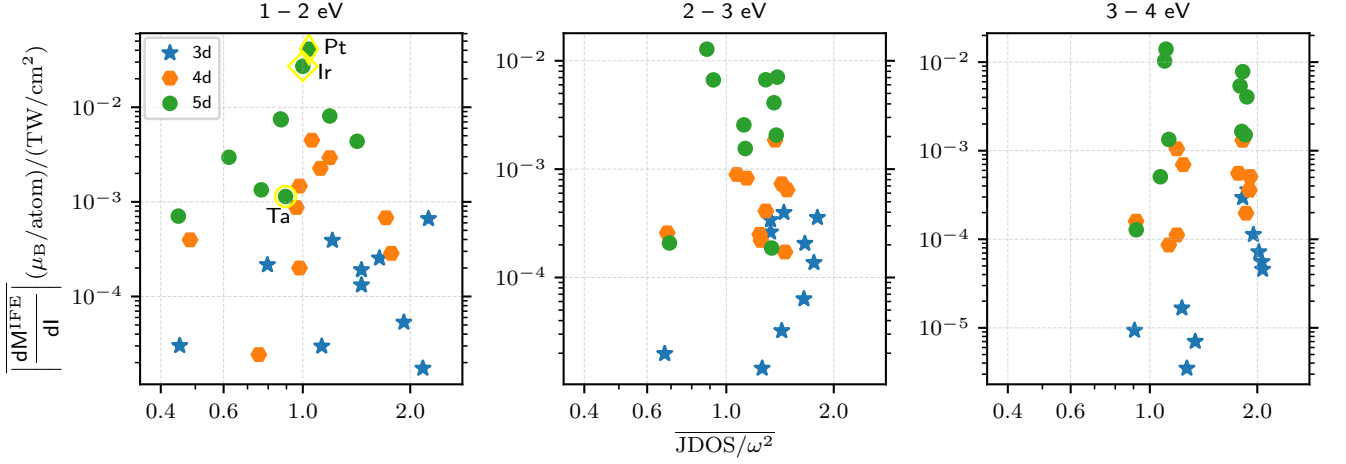


FIG. 3. Relationship of the mean absolute values of IFE,  $M^{\text{IFE}}$  with their  $\text{JDOS}/\omega^2$  for  $3d$ ,  $4d$  and  $5d$  metals in the frequency range 1–2 eV (left), 2–3 eV (middle) and 3–4 eV (right). The vertical scale is logarithmic.

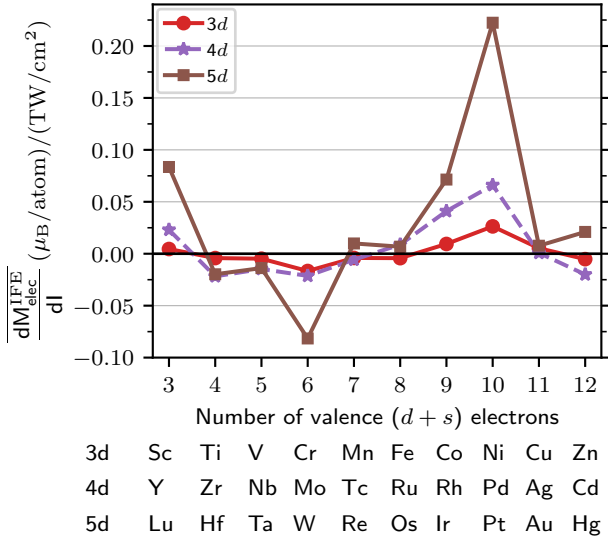


FIG. 4. Calculated mean value of  $M_{\text{elec}}^{\text{IFE}}$  for  $3d$ ,  $4d$  and  $5d$  metals in the 1–2 eV frequency range with periodic filling of valence states.

tions. For simplicity, we focus on the 1–2 eV frequency range, but this analysis can be extended to the 2–3 eV and 3–4 eV ranges.

#### D. Investigation of $M_{\text{elec}}^{\text{IFE}}$ and its correlation with spin-Hall conductivity (SHC)

Figure 4 shows the mean value of doubly-resonant electron IFE ( $M_{\text{elec}}^{\text{IFE}}$ ) with increasing valence electrons in the 1–2 eV frequency range. The general trend of  $M_{\text{elec}}^{\text{IFE}}$  is similar for  $3d$ ,  $4d$ , and  $5d$  metals, with a larger magnitude for  $5d$  metals due to the stronger SOC strength. The

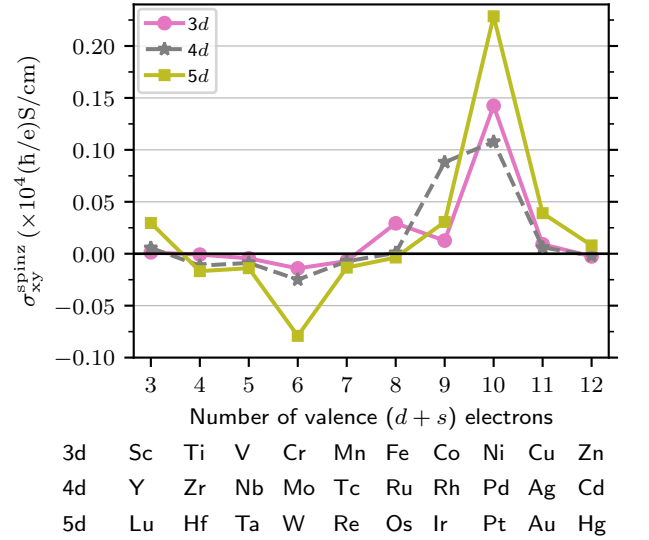


FIG. 5. The real part of spin hall conductivity (SHC)  $\sigma_{xy}^{\text{spin}}$  for  $3d$ ,  $4d$  and  $5d$  metals as function of valence electrons. The SHC is calculated at  $\omega=0$  at their respective Fermi energies using  $\eta=0.1$  eV.

sign of  $M_{\text{elec}}^{\text{IFE}}$  varies, being positive for some elements and negative for others, depending on the number of  $d$  electrons ( $n_d$ ). Specifically, except for group 3, elements with  $n_d \leq 5$  show negative values of  $M_{\text{elec}}^{\text{IFE}}$ , while elements with  $n_d > 5$  have positive values. We observe that group 6 metals such as Cr, Mo, and W, with exactly half-filled  $d$  states, show higher negative values of  $M_{\text{elec}}^{\text{IFE}}$ , while group 10 metals such as Ni, Pd, and Pt, exhibit higher positive values, with Pt reaching the highest  $M_{\text{elec}}^{\text{IFE}}$  among all. This dependence of  $M_{\text{elec}}^{\text{IFE}}$  on valence electrons is similar to the well-known dependence of spin Hall conductivity (SHC) on valence electrons [20–24], making it relevant to

compare our calculated mean  $M_{\text{elec}}^{\text{IFE}}$  with SHC.

The SHC describes the generation of a transverse spin current in response to an applied electric field [25]. In our IFE study, we assume the electric field in the  $xy$ -plane, resulting in spin moments induced along the  $z$ -direction. Similarly, for SHC, an electric field in the  $xy$ -plane, induces spin polarization along the  $z$ -direction ( $\sigma_{xy}^{\text{spin}z}$ ). According to the Kubo formula, the SHC can be expressed as [39, 46, 47]

$$\sigma_{xy}^{\text{spin}z} = \hbar \int_{\text{BZ}} \frac{d^3k}{(2\pi)^3} \sum_n f_{n\mathbf{k}} \times \sum_{m \neq n} \frac{2 \text{Im} \left[ \langle \phi_{n\mathbf{k}} | \hat{j}_x^{\text{spin}z} | \phi_{m\mathbf{k}} \rangle \langle \phi_{m\mathbf{k}} | -e\hat{v}_y | \phi_{n\mathbf{k}} \rangle \right]}{(E_{m\mathbf{k}} - E_{n\mathbf{k}})^2 - (\hbar\omega + i\eta)^2}. \quad (4)$$

where  $f_{n\mathbf{k}}$  is the Fermi distribution function,  $\hat{j}_x^{\text{spin}z} = \frac{1}{2} \{ \hat{s}_z, \hat{v}_x \}$  is the spin current operator.

We calculate the SHC for 3d, 4d, and 5d metals at their respective Fermi energies with  $\omega = 0$ , as shown in Fig. 5. For consistency with our IFE calculations, a finite  $\eta = 0.1$  eV was used. Comparing Figs. 5 and 4 reveals that the SHC trend with valence electrons closely resembles that of  $M_{\text{elec}}^{\text{IFE}}$ . Like  $M_{\text{elec}}^{\text{IFE}}$ , SHC shows positive peaks for group 10 metals, such as Ni, Pd, and Pt, while group 6 metals, such as Cr, Mo, and W, exhibit negative peaks. Our SHC results align well with previous studies [22–24]. However, the total IFE, which includes subtle asymmetry electron-hole moments and non-doubly resonant contributions, does not directly correlate with SHC or JDOS as summarized in Table I.

### E. Relationship between $M_{\text{elec}}^{\text{IFE}}$ and $M_{\text{hole}}^{\text{IFE}}$

The  $M_{\text{elec}}^{\text{IFE}}$  represents spin moments due to the interaction of optically excited electrons with CP light, while  $M_{\text{hole}}^{\text{IFE}}$  corresponds to spin moments from the optical de-excitation process involving holes. Together, these electron and hole spin magnetic moments lead to the IFE. To examine how  $M_{\text{elec}}^{\text{IFE}}$  and  $M_{\text{hole}}^{\text{IFE}}$  relate to the valence electrons, we calculate the absolute values of the mean of  $M_{\text{elec}}^{\text{IFE}}$  and  $M_{\text{hole}}^{\text{IFE}}$  as shown in Fig. 6. For most elements, the average values of  $M_{\text{hole}}^{\text{IFE}}$  are proportional to  $M_{\text{elec}}^{\text{IFE}}$ , meaning an increase in  $M_{\text{elec}}^{\text{IFE}}$  generally corresponds to an increase in  $M_{\text{hole}}^{\text{IFE}}$ , and vice versa. However, due to spin-orbit interaction and intrinsic asymmetries in the valence and conduction bands, subtle differences arise between the moments of excited electrons and holes, often leading to the emergence of new quantum phases [48–50]. This asymmetry may stem from external sources such as impurities [50, 51], side jump phenomena [52], or skew scattering processes [25, 53, 54]. In this study, we focus on interband transitions, where the asymmetry in electron-hole magnetic moments arises primarily from spin-orbit interaction and band structure effects.

We compare the asymmetry between the doubly-resonant electron-hole spin moments ( $M_{\text{elec}}^{\text{IFE}} - M_{\text{hole}}^{\text{IFE}}$ ) with

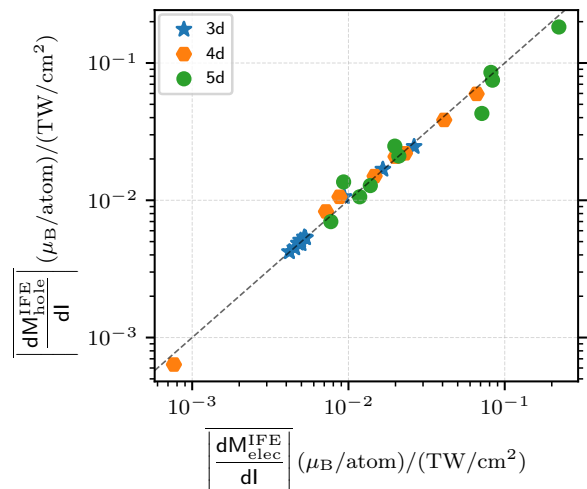


FIG. 6. Mean absolute values of  $M_{\text{hole}}^{\text{IFE}}$  versus  $M_{\text{elec}}^{\text{IFE}}$  for 3d, 4d and 5d metals in the 1–2 eV frequency range. Both axes are plotted on a logarithmic scale. The black dashed line serves as a guide to the eye.

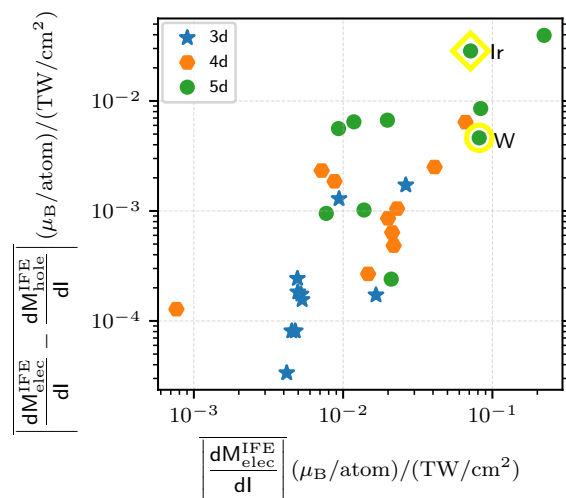


FIG. 7. Mean absolute values of the asymmetry in excited electron and hole spin magnetic moments ( $M_{\text{elec}}^{\text{IFE}} - M_{\text{hole}}^{\text{IFE}}$ ) against the mean absolute values of electron spin moments ( $M_{\text{elec}}^{\text{IFE}}$ ) for 3d, 4d, and 5d metals.

the excited electron spin moments ( $M_{\text{elec}}^{\text{IFE}}$ ). This relationship can also be extended to the hole IFE term ( $M_{\text{hole}}^{\text{IFE}}$ ). Figure 7 shows that, for most metals, the asymmetry in electron and hole magnetic moments ( $M_{\text{elec}}^{\text{IFE}} - M_{\text{hole}}^{\text{IFE}}$ ) differs significantly from  $M_{\text{elec}}^{\text{IFE}}$ . For instance, in most 3d metals,  $M_{\text{elec}}^{\text{IFE}}$  values are similar in magnitude, yet  $M_{\text{elec}}^{\text{IFE}} - M_{\text{hole}}^{\text{IFE}}$  values vary considerably. To illustrate, we highlight two representative 5d metals: W and Ir. For W,  $M_{\text{elec}}^{\text{IFE}}$  and  $M_{\text{hole}}^{\text{IFE}}$  are 0.082 and 0.085 ( $\mu_{\text{B}}/\text{atom})/(\text{TW}/\text{cm}^2)$ , respectively, while for Ir, they are 0.071 and 0.043 ( $\mu_{\text{B}}/\text{atom})/(\text{TW}/\text{cm}^2)$ , respectively.

Element symbol	Crystal structure	Lattice parameters		$\sigma_{xy}^{\text{spinz}}$ [ $\times 10^2$ ( $\hbar/e$ ) $S/cm$ ]	IFE [ $\times 10^{-3}$ ( $\mu_B/\text{atom})/(\text{TW}/\text{cm}^2)$ ]				
		$a$ ( $\text{\AA}$ )	$c$ ( $\text{\AA}$ )		$M_{\text{elec}}^{\text{IFE}}$	$M_{\text{hole}}^{\text{IFE}}$	$M_{\text{elec}}^{\text{IFE}} - M_{\text{hole}}^{\text{IFE}}$	$M_{\text{ndr}}^{\text{IFE}}$	$M^{\text{IFE}}$
Sc	hcp	3.31	5.27	0.135	4.532	-4.493	0.039	0.014	0.053
Ti	hcp	2.95	4.69	-0.085	-4.185	4.213	0.028	-0.034	-0.006
V	bcc	3.03		-0.441	-4.859	4.859	0.081	-0.054	0.027
Cr	bcc	2.91		-1.410	-16.632	16.804	0.172	-0.040	0.132
Mn	bcc	2.79		-0.705	-4.069	4.312	0.243	-0.052	0.191
Fe	bcc	2.87		2.928	-4.254	4.095	-0.159	-0.095	-0.254
Co	hcp	2.51	4.07	1.264	9.393	-10.553	-1.160	0.511	-0.649
Ni	fcc	3.52		14.244	26.317	-24.598	1.719	-1.328	0.391
Cu	fcc	3.61		0.908	5.305	-5.318	-0.012	-0.204	-0.216
Zn	hcp	2.66	4.95	-0.258	-5.218	5.392	0.175	-0.144	0.030
Y	hcp	3.64	5.73	0.559	23.20	-22.048	0.972	-0.304	0.668
Zr	hcp	3.23	5.15	-1.145	-21.754	21.877	0.123	-0.219	-0.097
Nb	bcc	3.30		-0.887	-14.747	15.015	0.268	-0.075	0.192
Mo	bcc	3.15		-2.493	-21.333	21.970	0.637	0.235	0.872
Tc	hcp	2.74	4.39	-0.731	-5.747	8.035	2.287	-0.052	2.236
Ru	hcp	2.71	4.28	0.081	8.763	-10.601	-1.838	0.365	-1.472
Rh	fcc	3.80		8.810	40.997	-38.492	2.506	0.428	2.934
Pd	fcc	3.89		10.780	60.055	-59.633	6.422	-1.939	4.484
Ag	fcc	4.09		0.610	0.764	-0.636	0.128	-0.152	-0.024
Cd	hcp	2.98	5.62	-0.187	-19.983	20.840	0.857	-0.459	0.397
La	hcp	3.50	5.55	2.961	83.514	-74.979	8.535	-0.455	8.080
Hf	hcp	3.20	5.05	-1.676	-19.780	24.815	5.034	-1.374	3.661
Ta	bcc	3.30		-1.394	-13.809	12.787	-1.022	-0.115	-1.137
W	bcc	3.17		-7.908	-81.573	85.365	3.792	3.585	7.377
Re	hcp	2.76	4.46	-1.337	9.893	-3.434	6.459	1.061	7.520
Os	hcp	2.73	4.32	-0.366	6.796	-12.411	-5.614	2.678	-2.936
Ir	fcc	3.84		3.060	71.406	-42.860	28.547	-1.410	27.137
Pt	fcc	3.92		22.859	222.402	-182.946	39.455	1.686	41.142
Au	fcc	4.08		3.907	7.709	-6.994	0.716	-1.627	-0.911
Hg	rhombohedral	4.47	3.04	0.802	20.993	-21.017	-0.024	-0.683	-0.707

$b = 4.09 \text{ \AA}$ ,  $\gamma = 84.4^\circ$

TABLE I. List of 30 elements considered in this work with their lattice parameters, SHC, the mean value of contributions to IFE, and total spin IFE in the 1–2 eV frequency range. The SHC data are scaled by  $10^{-2}$  while the IFE results are scaled by  $10^3$  factor.

The near symmetry between electron and hole moments in W results in a lower IFE, whereas the greater asymmetry in Ir leads to an IFE that is an order of magnitude higher. This demonstrates that a larger asymmetry in the effective magnetic moments of electrons and holes results in a higher IFE.

#### F. Classification by electron-hole spin asymmetry

Based on these results presented in the above sections and Table I, we intuitively categorize the spin IFE into four distinct cases illustrated in Fig. 8. In case I, elements exhibit high, but nearly equal magnitudes of excited electron and hole magnetic moments, leading to cancellation and a very low total IFE ( $M^{\text{IFE}}$ ) [Fig. 8(a)]. This category includes group 6 metals, such as Cr, Mo, and W, where the  $d$  orbitals are half-filled. As shown in Fig. 4,

$M_{\text{elec}}^{\text{IFE}}$  is large, but the total IFE remains small, as shown in Fig. 2.

Case II includes elements with large  $M_{\text{elec}}^{\text{IFE}}$  and  $M_{\text{hole}}^{\text{IFE}}$  values but with greater asymmetry between them [Fig. 8(b)]. Group 10 metals, such as Ni, Pd, and Pt, fall into this category. Case III involves elements with smaller  $M_{\text{elec}}^{\text{IFE}}$  and  $M_{\text{hole}}^{\text{IFE}}$  values but with a pronounced asymmetry, leading to a relatively large IFE [Fig. 8(c)]. An example is hcp Os, which despite having lower  $M_{\text{elec}}^{\text{IFE}}$  and  $M_{\text{hole}}^{\text{IFE}}$  values than bcc W, displays higher total IFE in the 2–4 eV frequency range due to the greater asymmetry in electron-hole moments.

Case IV is trivial, where both low magnitudes and low asymmetry between  $M_{\text{elec}}^{\text{IFE}}$  and  $M_{\text{hole}}^{\text{IFE}}$  leads to a lower total IFE [see Fig. 8(d)]. Group 12 metals, such as Zn, Cd, and Hg, which have filled  $d$  and  $s$  orbitals fall into this category. These elements exhibit high symmetry between electron and hole spin moments, resulting in small  $M^{\text{IFE}}$ .

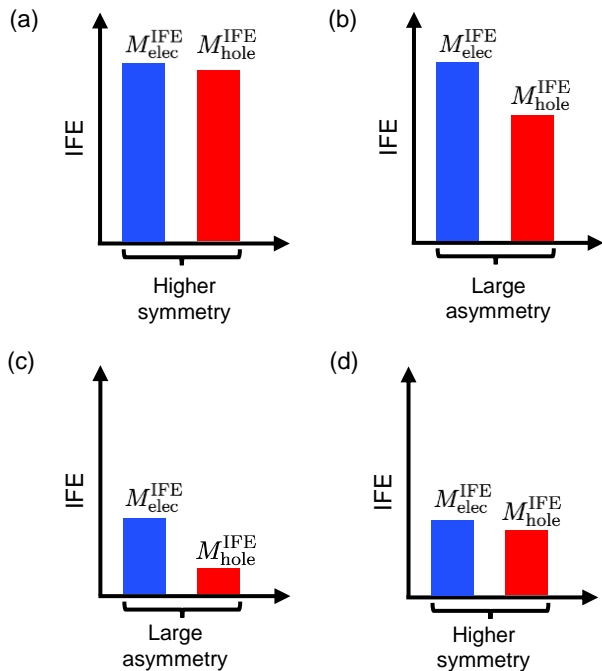


FIG. 8. Schematic representation of the spin-induced IFE in nonmagnetic metals, categorized into four cases. (a) Case I: Large  $M_{\text{elec}}^{\text{IFE}}$  and  $M_{\text{hole}}^{\text{IFE}}$  with near cancellation, resulting in low  $M^{\text{IFE}}$ . (b) Case II: Large  $M_{\text{elec}}^{\text{IFE}}$  and  $M_{\text{hole}}^{\text{IFE}}$  with significant asymmetry. (c) Case III: Smaller  $M_{\text{elec}}^{\text{IFE}}$  and  $M_{\text{hole}}^{\text{IFE}}$  with larger asymmetry. (d) Case IV: Small  $M_{\text{elec}}^{\text{IFE}}$ ,  $M_{\text{hole}}^{\text{IFE}}$ , and low asymmetry, resulting in low  $M^{\text{IFE}}$ . Figures not drawn to scale.

The observed asymmetry between electron and hole moments arises from differences in the valence and conduction band structures. Valence bands are predominantly  $d$ -state driven, while the conduction bands are primarily  $s$ -state driven, leading to different SOC strengths. As SOC increases with atomic number, both the asymmetry in electron-hole spin moments and the IFE increase. Therefore,  $5d$  metals exhibit higher IFE values compared to their  $3d$  and  $4d$  counterparts higher up in the periodic table.

### G. Band structure engineering and IFE

To further investigate the IFE trend with valence electrons, we calculated the IFE while tuning the Fermi levels of the transition metals maintaining the same crystal structure. The periodic arrangement of transition metals is governed by the filling of their  $d$  and  $s$  orbitals, which play a key role in defining both crystal structures [55] and the IFE variations.

For bcc crystals, we compared Ta and W, which have similar valence electron states and hopping values, resulting in nearly identical band structures, as shown in Figs. 9(a) and 9(b). The main difference lies in their electron densities and the position of the Fermi level ( $E_F$ ), indicated by the dashed black lines. Due to the differ-

ences in valence electrons, the IFEs of Ta and W vary significantly [see Figs. 9(c) and 9(e)]. By shifting the  $E_F$  of Ta upwards by 1.9 eV, we adjusted the valence electrons to match those of W. As a result, the frequency dependence of IFE for Ta with the shifted  $E_F$  resembles that of W [Fig. 9(d)]. The decomposition of IFE into doubly-resonant and non-doubly-resonant terms are also similar, with minor discrepancies near  $\hbar\omega = 2.5\text{--}4.0$  eV attributed to differences in lattice parameters and slight variations in SOC strength between Ta and W.

For fcc crystals, we demonstrate the similarity in IFE among Ir, Pt, and Au, by rigidly shifting their Fermi levels. Figure 10 shows that the IFE of Pt can be made analogous to that of Ir and Au, each with nine and eleven valence electrons, respectively. A similar equivalence in IFE has been demonstrated for hcp- $T_c$  and hcp-Ru crystals as shown in Fig. 14 of Appendix B, underscoring the important role of band structure engineering in tuning spin IFE. In practice, such Fermi-level shifts can be achieved through chemical doping or alloying.

## V. SUMMARY

In summary, we investigated the spin contributions to the IFE in  $3d$ ,  $4d$ , and  $5d$  transition metals. The IFE depends on the asymmetry in excited electron and hole spin magnetic moments, which arises from differences in their band structures and the effects of spin-orbit coupling. Greater asymmetry leads to higher IFE values. We found that the trend in doubly-resonant electron IFE ( $M_{\text{elec}}^{\text{IFE}}$ ) with valence electrons aligns with the trend of spin Hall conductivity (SHC). Like SHC, the sign of  $M_{\text{elec}}^{\text{IFE}}$  depends on the number of valence electrons. However, the total spin IFE, which includes subtle asymmetries and non-doubly-resonant terms, does not correlate directly with SHC or JDOS. The SHC, IFE, and its decomposition terms are summarized in Table I.

Our results highlight Pt as having the highest IFE in the 1–2 eV frequency range, while Os exhibits the highest IFE in the 2–4 eV range with the opposite sign to Pt. We also showed that the IFEs of neighboring elements with similar crystal structures can be aligned by adjusting their Fermi levels. This study provides insight into the variation of spin contributions to the IFE as a function of valence electrons and offers a deeper understanding of the underlying physics of spin IFE. While our current focus is on the spin component of IFE, we anticipate that the orbital component [15, 24] will also play a significant role in future research.

## ACKNOWLEDGMENTS

The author acknowledges discussions with S. Coh. Computational resources were provided by the High-Performance Computing Center (HPCC) at UCR.



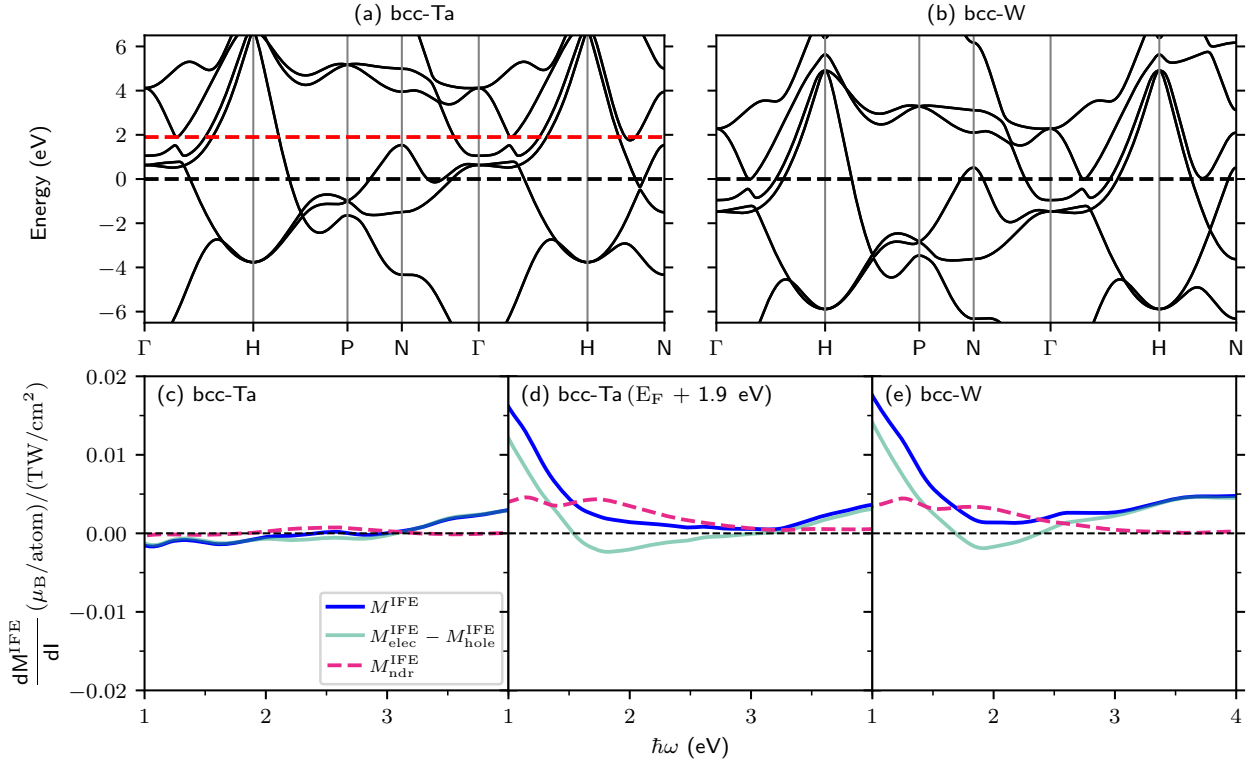


FIG. 9. Band structure of (a) bcc-Ta and (b) bcc-W, with the black dashed horizontal line representing  $E_F$ . The  $E_F$  of Ta shifted by 1.9 eV is marked with a red dashed line. (c–e) Calculated values of  $M^{\text{IFE}}$ ,  $M^{\text{IFE}}_{\text{elec}} - M^{\text{IFE}}_{\text{hole}}$ , and  $M^{\text{IFE}}_{\text{ndr}}$  for Ta at its actual  $E_F$ , Ta with  $E_F$  shifted by 1.9 eV, and W at its actual  $E_F$ , respectively.

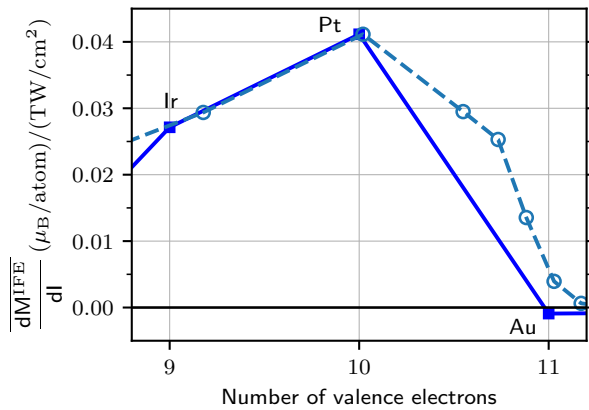


FIG. 10. Comparison of the mean of absolute IFE for fcc-Pt with varying the number of electrons by shifting the Fermi level, represented by the light blue open circles. The blue solid squares indicate the IFE values at their actual Fermi energies.

#### Appendix A: IFE as a function of frequency of light

Figure 11-13 show the spin IFE  $M^{\text{IFE}}$  (Eq. (1)) and its decomposition into doubly-resonant electron-hole IFE ( $M^{\text{IFE}}_{\text{elec}} - M^{\text{IFE}}_{\text{hole}}$ ) and non-doubly-resonant ( $M^{\text{IFE}}_{\text{ndr}}$ ) com-

ponents for 3d, 4d and 5d metals, arranged by increasing atomic number. For ferromagnetic Fe, Co, and Ni, non-magnetic structures are used.  $M^{\text{IFE}}$  increases with the valence electrons, with exceptions for filled shells, like Zn. In metals with five or fewer  $d$  electrons  $\leq 5$ , doubly-resonant terms dominate. Further, contributions from doubly-resonant and non-doubly-resonant are mostly opposite in sign. For Zn, these contributions nearly cancel each other, resulting in negligible IFE.

For some cases, such as fcc Ni and Cu, the non-doubly-resonant term is comparable to the doubly-resonant term. Cu shows higher values for  $\hbar\omega = 3-4$  eV due to  $d \rightarrow s$  interband resonance. Elements with lower  $d$  electron density, such as Sc and Ti, exhibit negligible  $M^{\text{IFE}}$ . For Cr, with half-filled  $d$  orbitals,  $M^{\text{IFE}}_{\text{elec}}$  and  $M^{\text{IFE}}_{\text{hole}}$  are large, whereas these values decrease for Mn, indicating dependence on  $d$  electron configuration. Similar observations were made for spin-Hall angle predictions of 3d metals [21].

In 4d metals,  $M^{\text{IFE}}$  increases with valence electrons up to Pd, with ten electrons in  $d$  and  $s$  orbitals, then decreases for Ag and Cd. In 5d elements, the non-doubly-resonant term is typically smaller, resulting in higher overall IFE values due to stronger SOC. Pt shows the highest  $M^{\text{IFE}}$ , followed by Ir in the 1–2 eV range, while Os exhibits the largest  $M^{\text{IFE}}$  in the 2–4eV range. Fully-filled configurations, like Hg in 5d metals, yield minimal

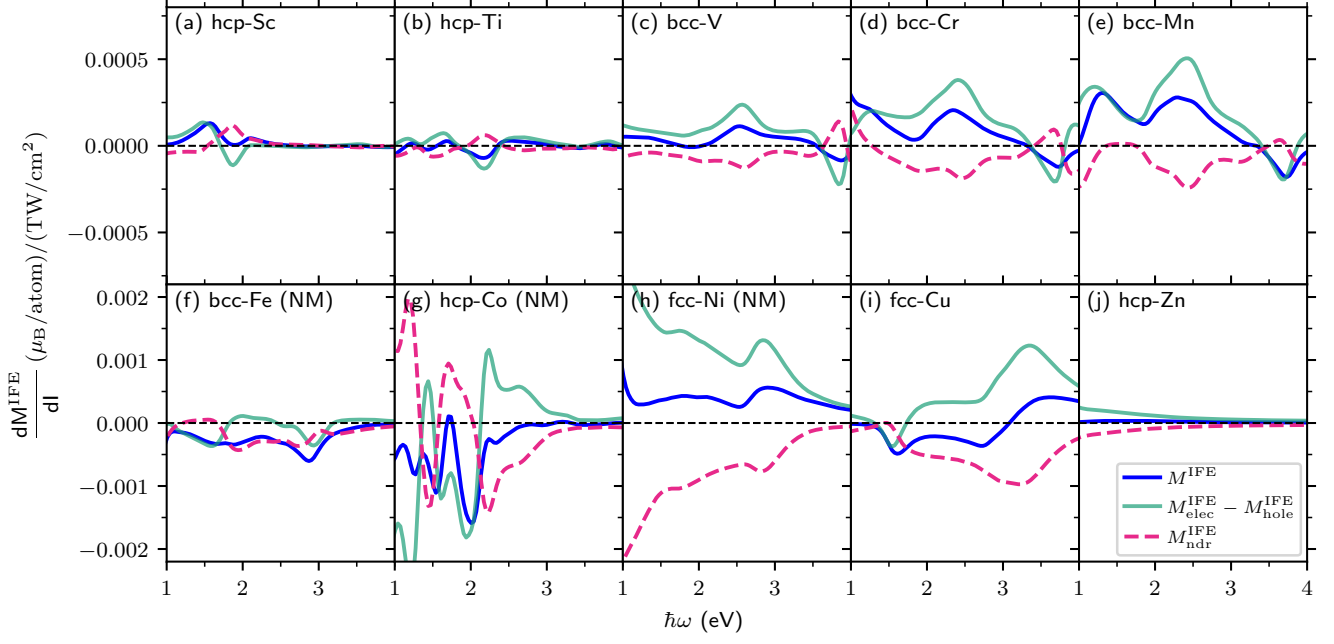


FIG. 11. Frequency dependence of the spin IFE ( $M^{\text{IFE}}$ ) for  $3d$  metals. The decomposition into doubly-resonant electron-hole ( $M_{\text{elec}}^{\text{IFE}} - M_{\text{hole}}^{\text{IFE}}$ ) and non-doubly resonant ( $M_{\text{ndr}}^{\text{IFE}}$ ) contributions is shown. In this study, we assumed nonmagnetic (NM) structures for Fe, Co, and Ni, resulting in double degenerate bands.

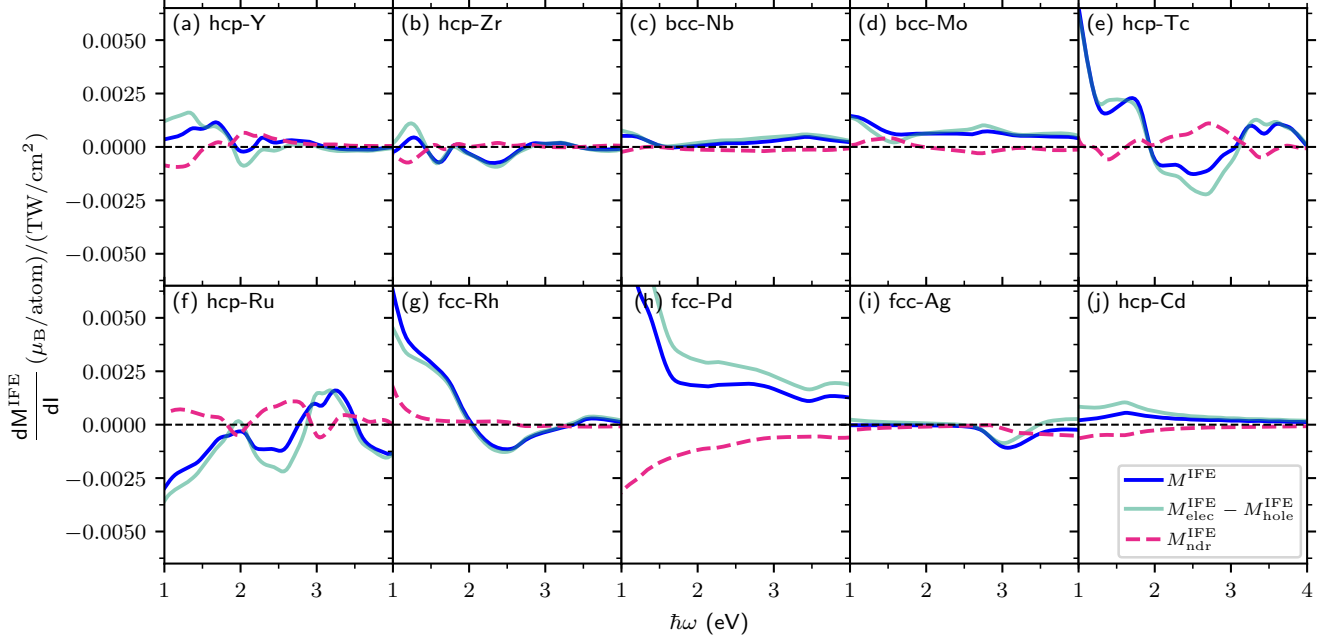


FIG. 12. Frequency dependence of  $M^{\text{IFE}}$  and its decomposition into doubly-resonant term  $M_{\text{elec}}^{\text{IFE}} - M_{\text{hole}}^{\text{IFE}}$ , and non-doubly-resonant term  $M_{\text{ndr}}^{\text{IFE}}$  for  $4d$ -metals.

IFE, similar to filled-shell  $3d$  and  $4d$  metals.

#### Appendix B: IFE in hcp metals by Fermi level tuning

Figure 14 shows the equivalence of IFE of hcp-Tc and hcp-Ru, by shifting Fermi levels of Ru by 1.5 eV.

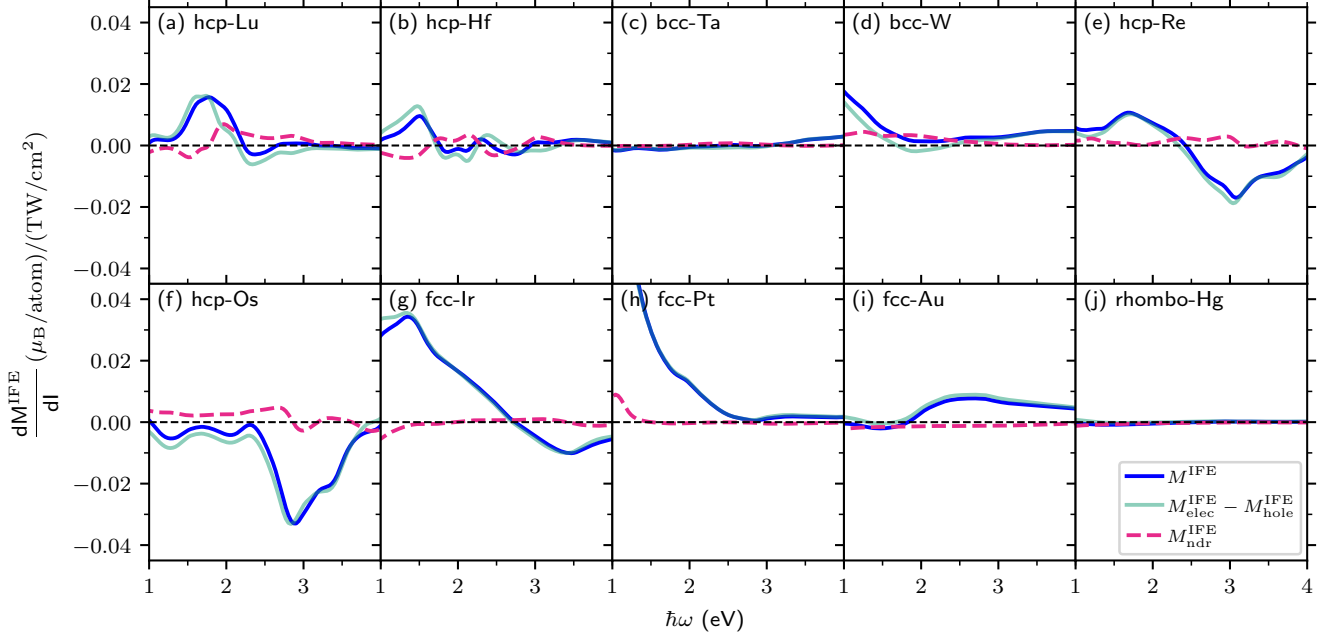


FIG. 13. Frequency dependence of  $M^{\text{IFE}}$  and its decomposition into doubly-resonant term  $M_{\text{elec}}^{\text{IFE}} - M_{\text{hole}}^{\text{IFE}}$ , and non-doubly-resonant term  $M_{\text{ndr}}^{\text{IFE}}$  for 5d-metals.

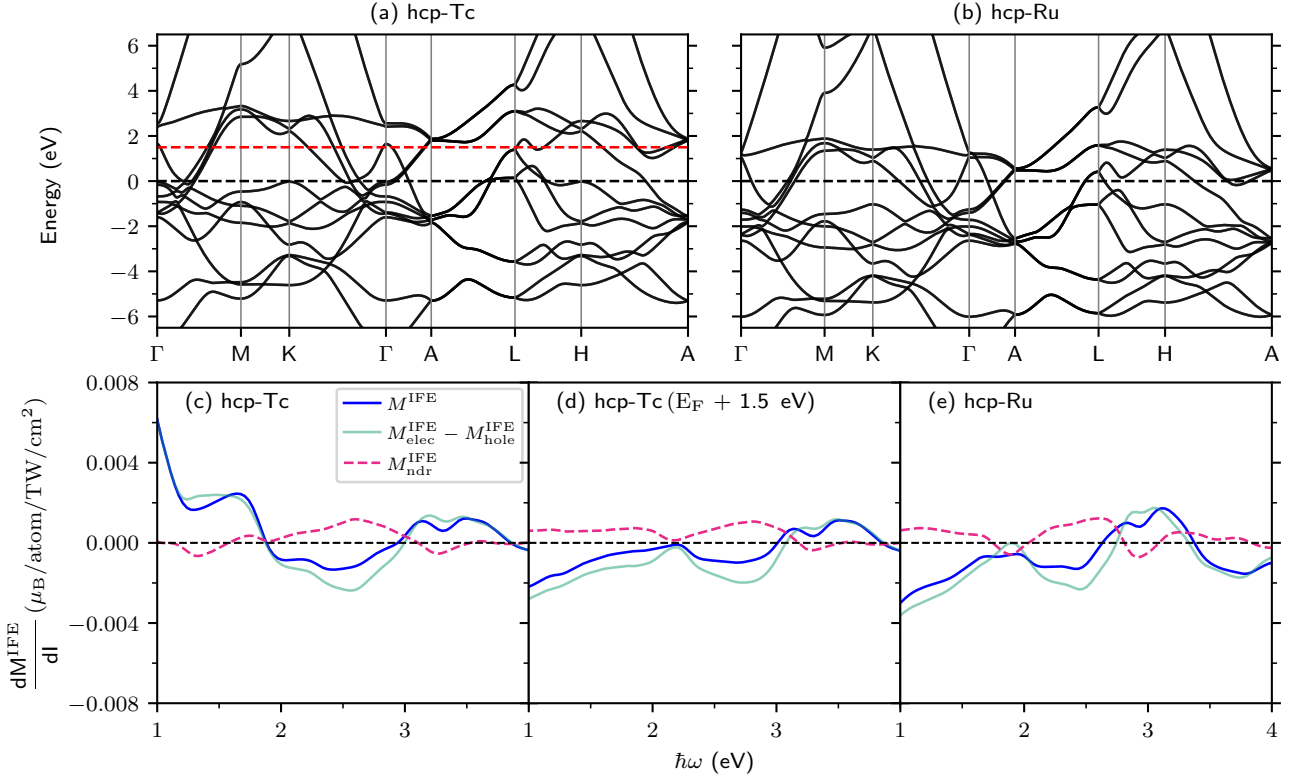


FIG. 14. Band structure of (a) hcp-Tc and (b) hcp-Ru, with actual  $E_F$ . The  $E_F$  of Tc shifted by 1.5 eV is represented by red dashed line. (c–e) Calculated values of IFE and its components for Tc at its actual  $E_F$ , Tc with  $E_F$  shifted by 1.5 eV, and Ru at its actual  $E_F$ , respectively.

- [1] J. P. van der Ziel, P. S. Pershan, and L. D. Malmstrom, Optically-induced magnetization resulting from the inverse Faraday effect, *Phys. Rev. Lett.* **15**, 190 (1965).
- [2] P. S. Pershan, J. P. van der Ziel, and L. D. Malmstrom, Theoretical discussion of the inverse Faraday effect, raman scattering, and related phenomena, *Phys. Rev.* **143**, 574 (1966).
- [3] S. Alebrand, M. Gottwald, M. Hehn, D. Steil, M. Cinchetti, D. Lacour, E. E. Fullerton, M. Aeschlimann, and S. Mangin, Light-induced magnetization reversal of high-anisotropy TbCo alloy films, *Appl. Phys. Lett.* **101**, 162408 (2012).
- [4] C.-H. Lambert, S. Mangin, B. S. D. C. S. Varaprasad, Y. K. Takahashi, M. Hehn, M. Cinchetti, G. Malinowski, K. Hono, Y. Fainman, M. Aeschlimann, and E. E. Fullerton, All-optical control of ferromagnetic thin films and nanostructures, *Science* **345**, 1337 (2014).
- [5] S. Mangin, M. Gottwald, C.-H. Lambert, D. Steil, V. Uhler, L. Pang, M. Hehn, S. Alebrand, M. Cinchetti, G. Malinowski, Y. Fainman, M. Aeschlimann, and E. E. Fullerton, Engineered materials for all-optical helicity-dependent magnetic switching, *Nat. Mater* **13**, 286 (2014).
- [6] A. V. Kimel, A. Kirilyuk, P. A. Usachev, R. V. Pisarev, A. M. Balbashov, and T. Rasing, Ultrafast non-thermal control of magnetization by instantaneous photomagnetic pulses, *Nature* **435**, 655 (2005).
- [7] C. D. Stanciu, F. Hansteen, A. V. Kimel, A. Kirilyuk, A. Tsukamoto, A. Itoh, and T. Rasing, All-optical magnetic recording with circularly polarized light, *Phys. Rev. Lett.* **99**, 047601 (2007).
- [8] G. M. Choi, A. Schleife, and D. G. Cahill, Optical-helicity-driven magnetization dynamics in metallic ferromagnets, *Nat. Comm.* **8** (2017).
- [9] A. Kirilyuk, A. V. Kimel, and T. Rasing, Ultrafast optical manipulation of magnetic order, *Rev. Mod. Phys.* **82**, 2731 (2010).
- [10] O. H.-C. Cheng, D. H. Son, and M. Sheldon, Light-induced magnetism in plasmonic gold nanoparticles, *Nat. Photon* **14**, 365 (2020).
- [11] V. H. Ortiz, S. B. Mishra, L. Vuong, S. Coh, and R. B. Wilson, Specular inverse Faraday effect in transition metals, *Phys. Rev. Mater.* **7**, 125202 (2023).
- [12] L. P. Pitaevskii, Electric Forces in a Transparent Dispersive Medium, *Sov. Phys. JETP* **12**, 1450 (1961).
- [13] P. S. Pershan, Nonlinear optical properties of solids: Energy considerations, *Phys. Rev.* **130**, 919 (1963).
- [14] R. Hertel, Theory of the inverse Faraday effect in metals, *J. Magn. Magn. Mater.* **303**, L1 (2006).
- [15] M. Berritta, R. Mondal, K. Carva, and P. M. Oppeneer, Ab initio theory of coherent laser-induced magnetization in metals, *Phys. Rev. Lett.* **117**, 137203 (2016).
- [16] F. Freimuth, S. Blügel, and Y. Mokrousov, Laser-induced torques in metallic ferromagnets, *Phys. Rev. B* **94**, 144432 (2016).
- [17] P. Scheid, G. Malinowski, S. Mangin, and S. Lebègue, Ab initio theory of magnetization induced by light absorption in ferromagnets, *Phys. Rev. B* **100**, 214402 (2019).
- [18] P. Scheid, S. Sharma, G. Malinowski, S. Mangin, and S. Lebègue, Ab initio study of helicity-dependent light-induced demagnetization: From the optical regime to the extreme ultraviolet regime, *Nano Lett.* **21**, 1943 (2021).
- [19] S. B. Mishra and S. Coh, Spin contribution to the inverse Faraday effect of nonmagnetic metals, *Phys. Rev. B* **107**, 214432 (2023).
- [20] T. Tanaka, H. Kontani, M. Naito, T. Naito, D. S. Hirashima, K. Yamada, and J. Inoue, Intrinsic spin Hall effect and orbital Hall effect in  $4d$  and  $5d$  transition metals, *Phys. Rev. B* **77**, 165117 (2008).
- [21] C. Du, H. Wang, F. Yang, and P. C. Hammel, Systematic variation of spin-orbit coupling with  $d$ -orbital filling: Large inverse spin Hall effect in  $3d$  transition metals, *Phys. Rev. B* **90**, 140407 (2014).
- [22] D. Jo, D. Go, and H.-W. Lee, Gigantic intrinsic orbital Hall effects in weakly spin-orbit coupled metals, *Phys. Rev. B* **98**, 214405 (2018).
- [23] L. Salemi and P. M. Oppeneer, First-principles theory of intrinsic spin and orbital Hall and Nernst effects in metallic monoatomic crystals, *Phys. Rev. Mater.* **6**, 095001 (2022).
- [24] D. Go, H.-W. Lee, P. M. Oppeneer, S. Blügel, and Y. Mokrousov, First-principles calculation of orbital Hall effect by Wannier interpolation: Role of orbital dependence of the anomalous position, *Phys. Rev. B* **109**, 174435 (2024).
- [25] J. Sinova, S. O. Valenzuela, J. Wunderlich, C. H. Back, and T. Jungwirth, Spin Hall effects, *Rev. Mod. Phys.* **87**, 1213 (2015).
- [26] R. Karplus and J. M. Luttinger, Hall effect in ferromagnetics, *Phys. Rev.* **95**, 1154 (1954).
- [27] M. Battiato, G. Barbalinardo, and P. M. Oppeneer, Quantum theory of the inverse Faraday effect, *Phys. Rev. B* **89**, 014413 (2014).
- [28] D. Popova, A. Bringer, and S. Blügel, Theory of the inverse Faraday effect in view of ultrafast magnetization experiments, *Phys. Rev. B* **84**, 214421 (2011).
- [29] R. J. Elliott, Theory of the effect of spin-orbit coupling on magnetic resonance in some semiconductors, *Phys. Rev.* **96**, 266 (1954).
- [30] F. Pientka, M. Gradhand, D. V. Fedorov, I. Mertig, and B. L. Györfly, Gauge freedom for degenerate Bloch states, *Phys. Rev. B* **86**, 054413 (2012).
- [31] P. Giannozzi and *et al.*, Advanced capabilities for materials modelling with Quantum ESPRESSO, *J. Phys.: Condens. Matter* **29**, 465901 (2017).
- [32] J. P. Perdew, K. Burke, and M. Ernzerhof, Generalized gradient approximation made simple, *Phys. Rev. Lett.* **77**, 3865 (1996).
- [33] D. R. Hamann, Optimized norm-conserving Vanderbilt pseudopotentials, *Phys. Rev. B* **88**, 085117 (2013).
- [34] M. van Setten, M. Giantomassi, E. Bousquet, M. Verstraete, D. Hamann, X. Gonze, and G.-M. Rignanese, The pseudodojo: Training and grading a 85 element optimized norm-conserving pseudopotential table, *Comput. Phys. Commun.* **226**, 39 (2018).
- [35] G. Pizzi and *et al.*, Wannier90 as a community code: new features and applications, *J. Phys.: Condens. Matter* **32**, 165902 (2020).
- [36] N. Marzari, A. A. Mostofi, J. R. Yates, I. Souza, and D. Vanderbilt, Maximally localized Wannier functions: Theory and applications, *Rev. Mod. Phys.* **84**, 1419 (2012).

- [37] S. S. Tsirkin, High performance Wannier interpolation of berry curvature and related quantities with Wannierberri code, *Npj Comput. Mater.* **7**, 33 (2021).
- [38] X. Wang, J. R. Yates, I. Souza, and D. Vanderbilt, Ab initio calculation of the anomalous Hall conductivity by Wannier interpolation, *Phys. Rev. B* **74**, 195118 (2006).
- [39] J. Qiao, J. Zhou, Z. Yuan, and W. Zhao, Calculation of intrinsic spin Hall conductivity by Wannier interpolation, *Phys. Rev. B* **98**, 214402 (2018).
- [40] D. Sarma, Nature of dependence of spin-orbit splittings on atomic number, in *Proc. Indian Acad. Sci.*, Vol. 90 (Springer, 1981) pp. 19–26.
- [41] K. V. Shanavas, Z. S. Popović, and S. Satpathy, Theoretical model for rashba spin-orbit interaction in  $d$  electrons, *Phys. Rev. B* **90**, 165108 (2014).
- [42] M.-L. Thèye, Investigation of the optical properties of au by means of thin semitransparent films, *Phys. Rev. B* **2**, 3060 (1970).
- [43] N. E. Christensen and B. O. Seraphin, Relativistic band calculation and the optical properties of gold, *Phys. Rev. B* **4**, 3321 (1971).
- [44] V. H. Ortiz, S. Coh, and R. B. Wilson, Magneto-optical kerr spectra of gold induced by spin accumulation, *Phys. Rev. B* **106**, 014410 (2022).
- [45] L. Uba, S. Uba, and V. N. Antonov, Magneto-optical kerr spectroscopy of noble metals, *Phys. Rev. B* **96**, 235132 (2017).
- [46] Y. Yao and Z. Fang, Sign changes of intrinsic spin Hall effect in semiconductors and simple metals: First-principles calculations, *Phys. Rev. Lett.* **95**, 156601 (2005).
- [47] G. Y. Guo, S. Murakami, T.-W. Chen, and N. Nagaosa, Intrinsic spin Hall effect in platinum: First-principles calculations, *Phys. Rev. Lett.* **100**, 096401 (2008).
- [48] N. Ashcroft and D. Mermin, *Solid State Physics* (Brooks/Cole Cengage Learning, Belmont, CA, 1976).
- [49] R. J. Gooding, K. J. E. Vos, and P. W. Leung, Theory of electron-hole asymmetry in doped CuO<sub>2</sub> planes, *Phys. Rev. B* **50**, 12866 (1994).
- [50] N. Dale, R. Mori, M. I. B. Utama, J. D. Denlinger, C. Stansbury, C. G. Fatuzzo, S. Zhao, K. Lee, T. Taniguchi, K. Watanabe, *et al.*, Correlation-driven electron-hole asymmetry in graphene field effect devices, *npj Quantum Mater.* **7**, 9 (2022).
- [51] K.-K. Bai, Y.-C. Wei, J.-B. Qiao, S.-Y. Li, L.-J. Yin, W. Yan, J.-C. Nie, and L. He, Detecting giant electron-hole asymmetry in a graphene monolayer generated by strain and charged-defect scattering via landau level spectroscopy, *Phys. Rev. B* **92**, 121405 (2015).
- [52] L. Berger, Application of the Side-Jump Model to the Hall Effect and Nernst Effect in Ferromagnets, *Phys. Rev. B* **5**, 1862 (1972).
- [53] J. E. Hirsch, Electron-hole asymmetry and superconductivity, *Phys. Rev. B* **68**, 012510 (2003).
- [54] M. Gradhand, D. V. Fedorov, P. Zahn, and I. Mertig, Extrinsic spin Hall effect from first principles, *Phys. Rev. Lett.* **104**, 186403 (2010).
- [55] H. L. Skriver, Crystal structure from one-electron theory, *Phys. Rev. B* **31**, 1909 (1985).